EES Catalysis

Accepted Manuscript

This article can be cited before page numbers have been issued, to do this please use: Y. Zhang, X. Zhan, Z. Wei, C. Wang, Z. Zheng, S. Mei, D. Song, M. Ma, X. Zhang, X. Yang, T. Zhou, J. Zeng, Y. Peng and Z. Deng, *EES Catal.*, 2025, DOI: 10.1039/D5EY00227C.

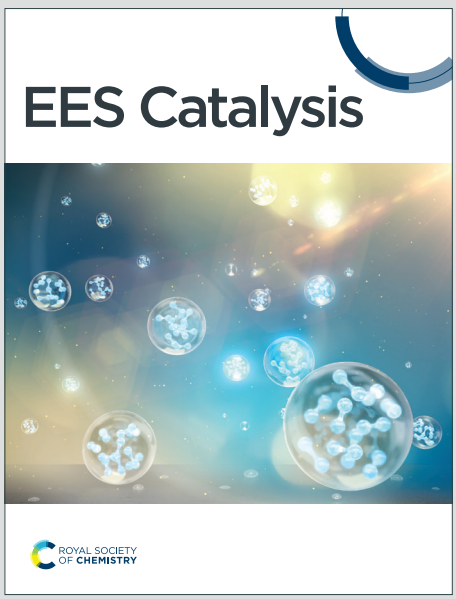

View Article Online
DOI: 10.1039/D5EY00227C

Broader context

Renewable-electricity-driven proton exchange membrane (PEM) water electrolysis for green hydrogen production has the advantages of high current density, high energy efficiency and fast response rate. Currently, the commonly used IrO_2 catalyst for the anode in PEM has bottlenecks such as low element reserves and high price. RuO_2 has relatively high OER activity, but its inherent instability under acidic OER conditions, primarily caused by Ru dissolution, severely limits practical applications. How to effectively suppress Ru dissolution, improve Ru utilization and stability remains a major challenge. In this work, taking advantage of the densely packed and stable crystalline structure of β-MnO_2 and dopant-induced lattice strain, we develop a polymer-mediated exsolution and segregation strategy to controllably expose Ru active sites on β-MnO_2 while mitigating dissolution through strong interfacial coupling. Advanced microscopic and spectroscopic studies unveil the Schottky mechanism for Ru exsolution and segregation, and the modulation of electronic structure through sacrificial pyrolysis of the polymer coating. Compared with traditional IrO_2 and RuO_2 catalysts, the Ru-MnO_2 catalyst invented here has the advantages of high Ru atom utilization and good stability, which can provide important theoretical and experimental basis for constructing low-precious-metal and long-life PEM water electrolysis devices.

View Article Online
DOI: 10.1039/D5EY00227C

ARTICLE

Polymer-mediated Exsolution and Segregation of Ruthenium Oxides on β-MnO_2 for Durable Water Oxidation in Proton-Exchange Membrane Electrolyzer

Received 00th January 20xx,
Accepted 00th January 20xx

DOI: 10.1039/x0xx00000x

Yanzhi Zhang,[+ab] Xingyi Zhan,[+ab] Zhihe Wei,[+ab] Chenghao Wang,[ab] Zhangyi Zheng,[ab] Shiwei Mei,[ab] Daqi Song,[ab] Mutian Ma,[ab] Xinyu Zhang,[ab] Xiya Yang,[ab] Tong Zhou,[ab] Jianrong Zeng,[cd] Yang Peng,*[ab] and Zhao Deng*[ab]

The development of acid-stable and low-noble-metal electrocatalysts for oxygen evolution reaction (OER) is challenging but demanding for large-scale application of proton-exchange membrane water electrolyzers (PEMWE). Herein, taking advantage of the densely packed and stable crystalline structure of β-MnO_2 and the dopant-induced lattice strain, a high-performance OER catalyst with low Ru loading is developed via the thermally-driven and polymer-mediated exsolution and segregation process. While high-resolution microscopic studies clearly illustrate the Schottky mechanism involved in the formation of polycrystalline RuO_x-containing grains anchored to the MnO_2 support, spectroscopic evidences unveil a significantly altered electronic structure with reduced Mn and Ru chemical states, as well as populated vacancies. Consequently, the best catalyst of Ru-MnO_2-PT achieves a remarkable OER activity in acidic medium, requiring an overpotential of only 163 mV to reach the current density of 10 mA cm^{-2}, in addition to a superb electrolytic stability, enabling a prolonged operation of PEMWE for over 2000 hours. This study sheds new light on controllably regulating the exsolution and segregation process of noble metal-doped transition metal oxides for the fabrication of highly robust OER catalysts.

Introduction

Renewables-powered water electrolysis has emerged as a cornerstone of the hydrogen economy, offering a sustainable pathway toward carbon neutrality.[1-4] Among the diverse water electrolysis technologies such as alkaline, acidic and solid oxide systems, proton exchange membrane water electrolyzer (PEMWE) distinguishes itself through merits of high operating current density (> 2 A cm^{-2}), high voltage efficiency (> 80%), rapid response (< 100 ms), and inherent adaptability to unstable energy inputs from solar/wind systems.[5, 6] However, in PEMWE the anodic oxygen evolution reaction (OER) under acidic condition imposes a critical challenge on the stability of electrocatalysts, demanding the use of noble metal oxides.[7-9] Currently, IrO_2 remains the benchmark OER catalyst in PEMWE due to its good catalytic activity and operational durability.[10] Yet, Iridium's scarcity (with annual global yield < 8 tons) and exorbitant cost (> US$ 150K kg^{-1}) hinder its large-scale application.[11] As an alternate, ruthenium (Ru) has a cost about 1/8 of that for Ir, but still contributes significantly to material expenses in PEMWE.[12, 13] Moreover, Ru-based catalysts suffer from oxidative dissolution under high OER potentials in acidic media, leading to irreversible performance degradation.[14] To enable cost-effective PEMWE deployment, it is imperative to reduce noble metal usage while enhancing catalyst longevity under harsh operational conditions.

Anchoring noble metal oxides on acid-stable supports is an effective strategy to achieve the goal above. To this end, researchers have devised various tactics, such as doping,[15-17] compositing,[18, 19] epitaxial growth,[20, 21] and interfacial engineering,[22, 23] targeting synergic activity-stability-cost improvement through multi-objective design. For instance, Ge et al. doped atomistic Ir into γ-MnO_2, and achieved superior activity and stability to commercial IrO_2 by promoting lattice oxygen participation and strengthening Ir–O covalency.[24] In a more recent study, Zhang et al. adopted a ripening-induced embedding strategy to anchor Ir nanoparticles onto cerium oxide by synchronizing the growth rate of the support with the nucleation rate of nanoparticles. This approach enabled long-term PEMWE operation while significantly reducing noble metal usage.[25] Despite these encouraging advances, further efforts are needed to continuously improve the catalyst durability while minimizing noble metal consumption in PEMWE.

[a.] Soochow Institute for Energy and Materials Innovations, Key Laboratory of Advanced Carbon Materials and Wearable Energy Technologies of Jiangsu Province, College of Energy, Soochow University, Suzhou 215006, P. R. China.
E-mail: zdeng@suda.edu.cn, ypeng@suda.edu.cn
[b.] Jiangsu Key Laboratory of Advanced Negative Carbon Technologies, Soochow University, Suzhou 215006, P. R. China.
[c.] Shanghai Synchrotron Radiation Facility, Shanghai Advanced Research Institute, Chinese Academy of Sciences, 201204 Shanghai, P. R. China.
[d.] Shanghai Institute of Applied Physics, Chinese Academy of Sciences, 201800 Shanghai, P. R. China.
[+.] These authors contributed equally to this work: Yanzhi Zhang, Xingyi Zhan, Zhihe Wei.
† Electronic Supplementary Information (ESI) available: [Experimental Section, supplementary figures and tables]. See DOI: 10.1039/x0xx00000x

Another promising approach to construct heterogeneous catalysts is through elemental exsolution and segregation.[26-28] Given a specific atmosphere, these processes occur when the segregation energy of one metal component in a multinary oxide matrix is lower than that of the others. Leveraging this "inside-out" mechanism, exsolved metal nanoparticles form uniformly on the oxide support, establishing strong interactions with the matrix.[29] This enhances interfacial electron transfer while preventing nanoparticle agglomeration under harsh reaction conditions. Moreover, the composition and morphology of the segregated phase can be finely tuned by adjusting the gas atmosphere and annealing conditions. To date the majority of oxide supports are limited to perovskites,[30, 31] layered double hydroxides (LDHs)[32, 33] and spinels,[34, 35] offering distinct advantages of high surface area, great thermal stability and superior metal nanoparticle dispersion. These exsolved nanoparticles acts as stable active sites during electrocatalysis, with the electronic structure effectively modulated by the underlying support.[36] However, most reported exsolution processes still require high temperature and lack precise control, posing challenges for structure regulation and scalable application.

In this study, we aim to reduce noble metal reliance and extend the longevity of oxygen evolution reaction (OER) catalysts in acidic media by employing MnO_2 as the oxide support to exsolve Ru-based active sites. The selection of β-MnO_2 is motivated by its densely packed lattice structure, wherein Ru doping could render a metastable state with significant lattice strain, thereby promoting thermally driven exsolution and segregation. Polymer coating is further applied to mediate the exsolution process through sacrificial pyrolysis. Using high-resolution microscopy and spectroscopy, we reveal the formation of polycrystalline RuO_x grains anchored on the MnO_2 support following the Schottky mechanism, concomitant with a significant change of the electronic structure. The optimized catalyst exhibits exceptional OER performance in acidic media, achieving a low overpotential of 163 mV at 10 mA cm^{-2} and outstanding stability, sustaining PEMWE operation for over 2000 hours. This work provides a new strategy for the controlled exsolution and segregation of noble metal-doped transition metal oxides, advancing the design and fabrication of highly durable OER catalysts.

Results and discussion

Theoretical prediction on the exsolution and segregation of Ru from β-MnO_2

By virtue of its 1 × 1 tunnel structure without support from any alkali/alkaline-earth cations, β-MnO_2 (Pyrolusite) is regarded as one of the most closely packed and thermodynamically stable polymorphs of manganese dioxide. Hence, one would envisage the difficulty to dope such a dense lattice with foreign cations, especially with larger radius. To assess the feasibility of Ru doping into β-MnO_2, we began by inspecting the energetics of the constructed Ru-MnO_2 models through density function theory (DFT) calculations. We first calculated the enthalpy changes for galvanically doping β-MnO_2 with Ru under both stressed and relaxed lattice conditions based on the atomic model shown in Fig. 1a. The results indicate a free

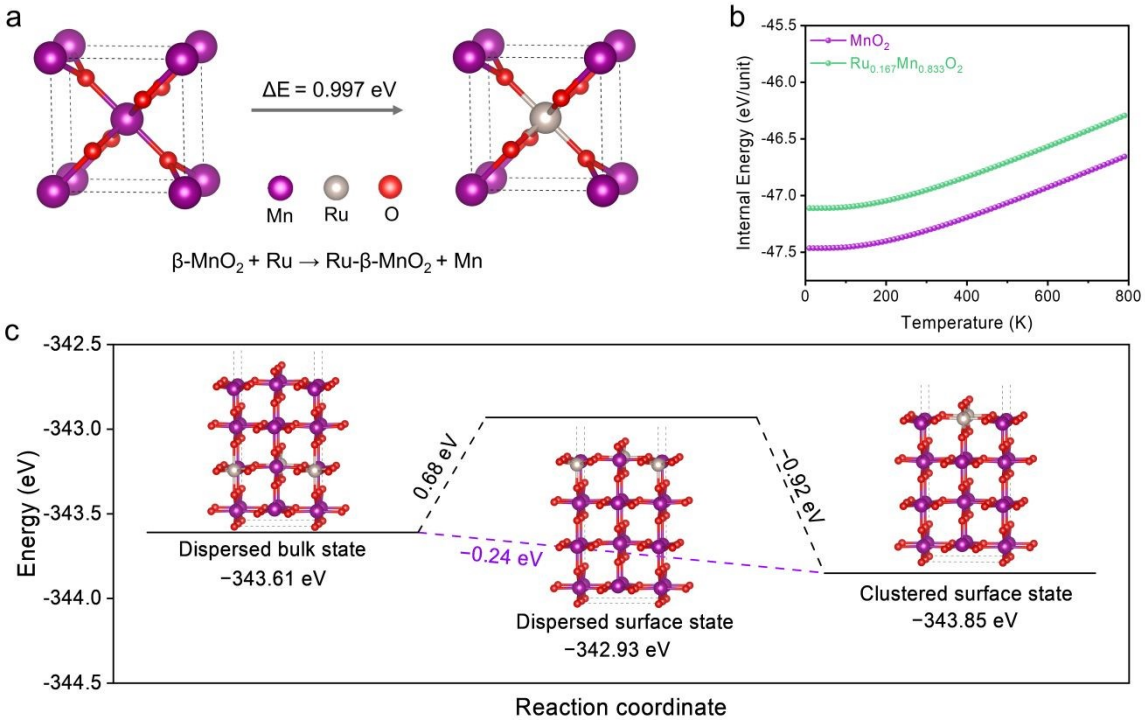

Fig. 1 DFT calculations on the energetics of Ru doping, exsolution and segregation in β-MnO_2. (a) Calculated enthalpy for galvanically replacing one Mn atom in β-MnO_2 with Ru (models are constrained to the lattice constant). (b) Temperature-dependent internal energy of MnO_2 and $Ru_{0.167}Mn_{0.833}O_2$. (c) Free energy change of Ru-MnO_2 transiting from the dispersed bulk state to dispersed surface state or clustered surface state.

View Article Online
DOI: 10.1039/D5EY00227C

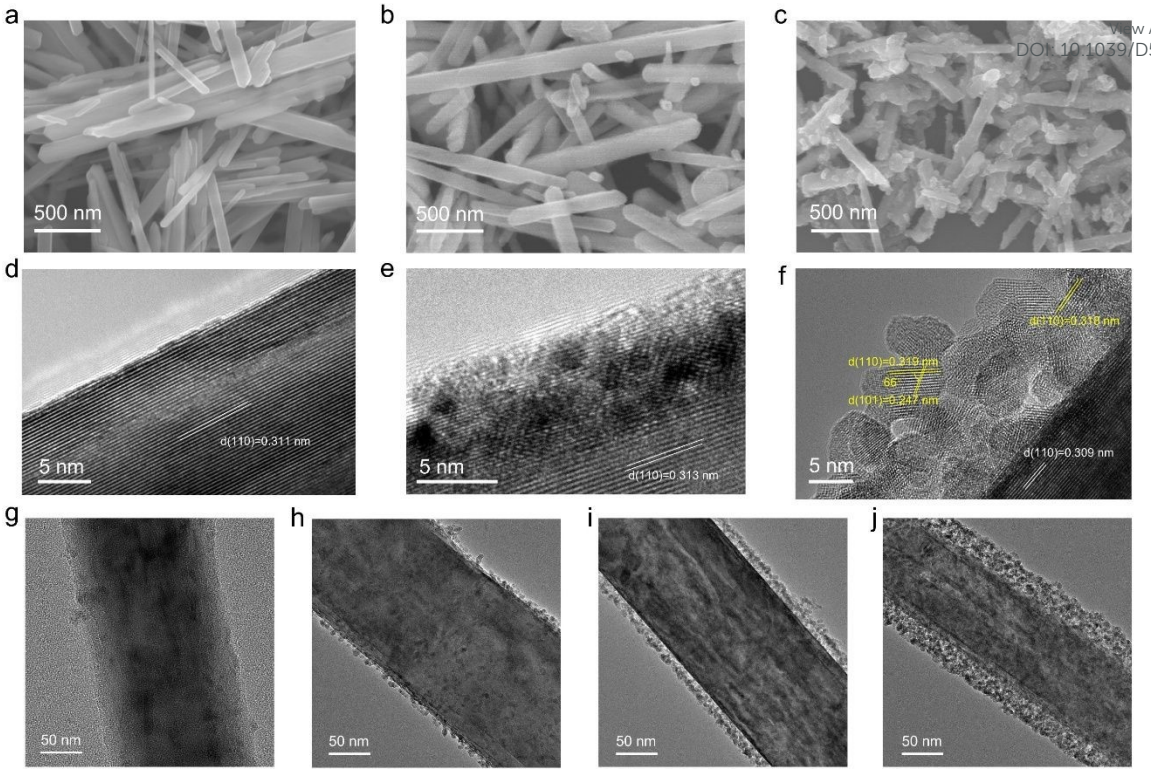

Fig. 2 Microscopic characterization of pristine and Ru-doped β-MnO_2 before and after thermal annealing. SEM images of (a) β-MnO_2, (b) Ru-MnO_2, and (c) Ru-MnO_2-T (60 min). TEM images of (d) β-MnO_2, (e) Ru-MnO_2, and (f) Ru-MnO_2-T (60 min). Lattice fringes labelled white correspond to β-MnO_2 while those labelled yellow belong to RuO_2. TEM images of Ru-MnO_2-T upon thermal annealing in air at 350 °C for (g) 0 min, (h) 30 min, (i) 60 min, and (j) 180 min.

energy increase of 0.997 eV for Ru-MnO_2 constrained to the lattice constant of β-MnO_2, in contrast to an exothermic process of −3.22 eV for the fully relaxed structure, of which the unit cell volume increased by 8.97% (Table S1 and Fig. S1, ESI†). Next, we calculated the internal energy of $Ru_{0.167}Mn_{0.833}O_2$ (with 1/6 of Mn in the lattice replaced by Ru), increasing by 0.35-0.36 eV per unit cell across the temperature range from 0 to 800 K (Fig. 1b and S2, ESI†). Apparently, the energy penalty caused by lattice strain far surpasses the enthalpy gain from the galvanic replacement reaction. These results support the feasibility of Ru doping into β-MnO_2 to form meta-stable Ru-MnO_2 at relatively mild conditions.

To interrogate the distribution of Ru atoms within the β-MnO_2 lattice, we compared six configurations of $Ru_{0.167}Mn_{0.833}O_2$ with varying Ru dispersity (Fig. S3, ESI†). The results indicate that, in general, the dispersed Ru arrangements exhibit lower free energies than those of clustered configurations, suggesting that Ru atoms tend to occupy discrete and isolated sites within the β-MnO_2 lattice to form a homogeneous solid solution. We then set to determine the minimal energy required to drive the dispersed bulk Ru atoms to surface. As shown in Fig. 1c, by reconfiguring the dispersed Ru atoms from their stressed bulk state to surface state, the free energy increased by 0.68 eV due to the offset of lattice strain by surface energy increase. However, when the surface Ru atoms are grouped together, the free energy of Ru-MnO_2 decreased by −0.92 eV, accounting for a total energy drop of −0.24 eV from the initial dispersed bulk state. Thus, the most probable scenario for Ru segregation from β-MnO_2 is transiting from the highly dispersed bulk state to aggregated surface state. Taken together from the calculation results, we posit that doping Ru into β-MnO_2 would result in a meta-stable state of Ru-MnO_2, requiring only a marginal energy input, such as modest thermal annealing, to drive Ru exsolution and segregation from the stressed MnO_2 lattice. As the atomic radius of Ru (178 pm) is slightly larger than that of Mn (161 pm), the extrusion of Ru atoms would disfavour the formation of Frankel defects but favour the Schottky defects (Fig. S4, ESI†).[37]

Thermally induced exsolution and segregation of Ru-MnO_2

Known for its capability in kinetic control of wet chemistry, microwave-assisted hydrothermal synthesis was employed to synthesize the metastable Ru-doped β-MnO_2. Compared to the conventional hydrothermal synthesis, microwave-assisted hydrothermal method typically shortens the reaction time, making industrial scaling-up attempting.[38,39] More detailed information about the synthetic procedure is given in the experimental section. Based on the elemental analysis using induction coupled plasma – atomic emission spectroscopy (ICP-AES), the highest Ru doping is limited to ~15% in mass percentage, which is implemented throughout the experimental studies here unless otherwise specified. Utilizing scanning electron microscopy (SEM) and high-resolution transmission electron microscopy (HR-TEM), we first compared the micro-morphology and lattice structure of the as-synthesized pristine β-MnO_2 (denoted as β-MnO_2), Ru-doped β-MnO_2 (denoted as Ru-MnO_2), and thermally treated Ru-MnO_2 (denoted as Ru-MnO_2-T). β-MnO_2 exhibited the typical nanorod structure with a smooth surface (Fig. 2a). TEM images (Fig. 2d and S5, ESI†)

showed the single-crystalline nature of these nanorods with characteristic (110) facets of 0.311 nm in d-spacing (JCPDS 24-0735). Ru-MnO_2 maintained the nanorod morphology of β-MnO_2, but with a slightly roughened surface (Fig. 2b). While (110) lattice fringes still dominated the crystals, polycrystalline features were also visualized, especially near the surface (Fig. 2e and S6, ESI†). Measurements on the (110) fringes revealed an average d-spacing of 0.313 nm, which is slightly larger than that of the pristine β-MnO_2. As the atomic radius of Ru is slightly larger than that of Mn, it was not odd to see the expanded and stressed lattice in Ru-doped MnO_2.

Upon thermal annealing in air at 350 °C for 1 hour, Ru-MnO_2-T developed a notably different morphology. Not only the nanorods became more fragmented, but also their surface appeared to be rougher (Fig. 2c). More strikingly, TEM images clearly revealed a newly developed surface layer comprising numerous polycrystalline grains (Fig. 2f and S7, ESI†). Most of these grains present only short-range order with discernable lattice fringes, while some are even amorphous. A careful inspection on the lattice constant and orientation found some of the crystalline grains can be assigned to RuO_2 (JCPDS 40-1290). Meanwhile, the inner MnO_2 (110) lattice spacing measured 0.309 nm (smaller than both of β-MnO_2 and Ru-MnO_2), indicating contraction of the bulk MnO_2 lattice due to the release of lattice strain caused by Ru segregation. Therefore, it is evident that thermal treatment of the meta-stable Ru-MnO_2 enables to drive the exsolution of Ru cations, which are then segregated and oxidized on the surface of β-MnO_2, forming MnO_2/RuO_2 heterostructures through the Schottky mechanism.[40]

The Ru exsolution and segregation from Ru-MnO_2 was further visualized via *ex situ* TEM images (Fig. 2g-j). After annealing for 30 mins, numerous small crystals of 5-10 nm emerged on the surface of β-MnO_2 (Fig. 2h and S8, ESI†). The number of these crystals continued to grow as the annealing time extended, coalescing to form a core-shell structure after 60 mins (Fig. 2i and S7, ESI†). By the end of the three-hour thermal treatment, the thickness of the surface layer, comprising loosely stacked and coalesced crystalline grains, was up to 30 nm (Fig. 2j and S9, ESI†). EDX elemental mapping images further confirmed the enrichment of Ru elements at the surface of β-MnO_2 rods for Ru-MnO_2-T as opposed to the homogeneous distribution of Ru in Ru-MnO_2 (Fig. S10, ESI†). These TEM observations enable us to conceive that Ru ions inside the MnO_2 lattice, driven by their high oxophilicity and high lattice strain, move towards the surface and leave vacancies behind. At the surface, the Ru ions are oxidized and aggregated to form RuO_2 clusters of varying crystallinity. With time, the vacancies propagate inward, contracting (or even collapsing) the β-MnO_2 lattice. This process makes the surface layer comprising a mixture of RuO_2 and MnO_2 crystals that are loosely attached to the shrunk β-MnO_2 base. Thus, from our comprehensive HR-TEM analysis, it is clear that the exsolution and segregation of Ru from β-MnO_2 follow the Schottky mechanism.

Polymer-mediated exsolution and segregation of RuO_x on β-MnO_2

Aiming to enhance the cementing of the segregated RuO_2 phase and the MnO_2 base, we coated the Ru-MnO_2 nanorods, prior to thermal treatment, with polyaniline to form an amorphous surface layer (denoted as Ru-MnO_2-P, Fig. 3a and S11, ESI†). Here, polyaniline was chosen for its suitable decomposition temperature (Fig. S12, ESI†), matching the annealing temperature of 350 °C used for Ru exsolution. The polyaniline-coated Ru-MnO_2 after thermal treatment (Ru-MnO_2-PT) also showed a roughened surface, but with more condensed

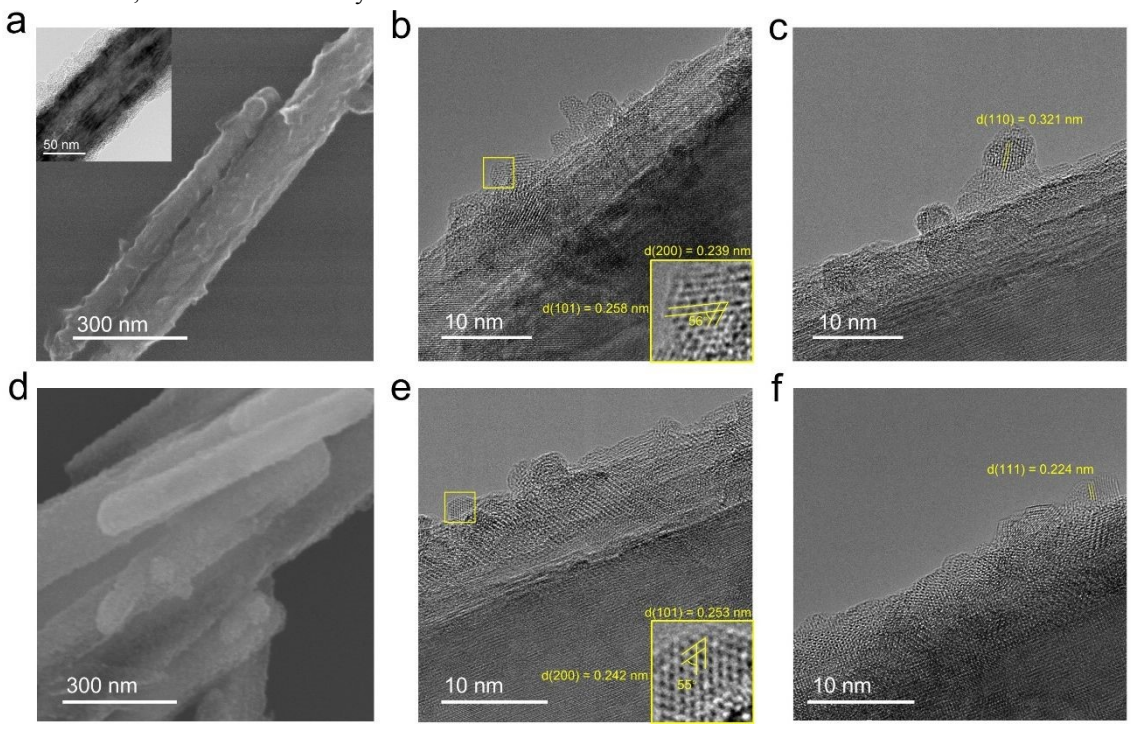

Fig. 3 Microscopic characterization of Ru-MnO_2-P and Ru-MnO_2-PT. (a) SEM and TEM (inset) images of Ru-MnO_2-P. (b)-(c) TEM images of Ru-MnO_2-PT (30 min). (d) SEM image of Ru-MnO_2-PT (180 min). (e)-(f) TEM images of Ru-MnO_2-PT (180 min).

View Article Online
DOI: 10.1039/D5EY00227C

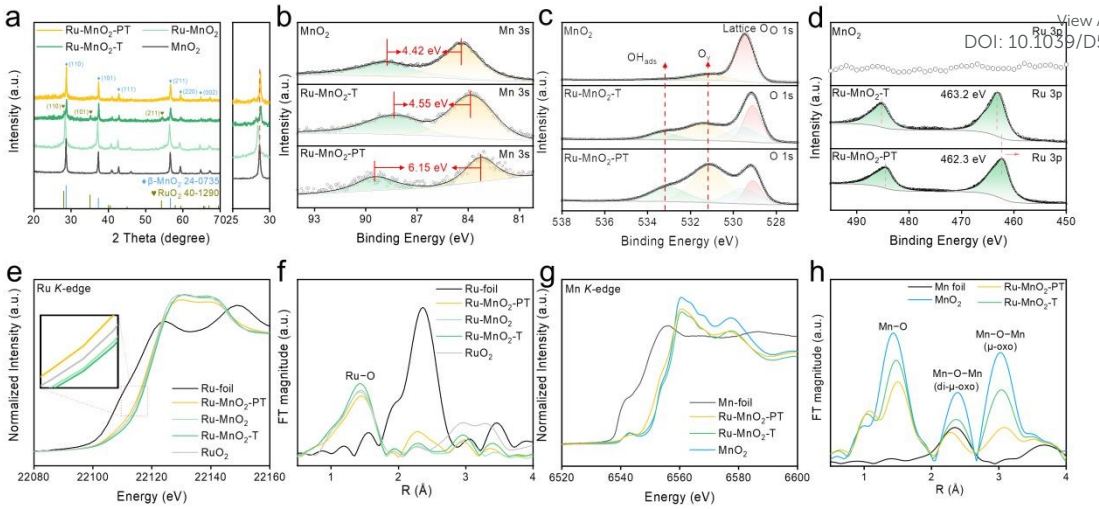

Fig. 4 Structural and electronic analyses. (a) XRD patterns of β-MnO_2, Ru-MnO_2, Ru-MnO_2-T, Ru-MnO_2-PT. The right panel amplifies the shift of the β-MnO_2(110) peaks. XPS (b) Mn 3s, (c) O 1s and (d) Ru 3p spectra taken on β-MnO_2, Ru-MnO_2-T and Ru-MnO_2-PT. (e) XANES Ru K-edge and (f) the corresponding FT-EXAFS spectra taken on Ru-MnO_2-T and Ru-MnO_2-PT in reference to RuO_2 and Ru foil. (g) XANES Mn K-edge and (h) the corresponding FT-EXAFS spectra taken on Ru-MnO_2-T and Ru-MnO_2-PT in reference to MnO_2 and Mn foil.

lattice structure (Fig. 3b-f). Combining HR-TEM, combustion test (Fig. S13, ESI†) and Raman analysis (Fig. S14, ESI†), we were able to conclude the complete pyrolysis of the PANI coating. A close inspection on the lattice fringes finds the surface layer is composed of mixed MnO_2 and RuO_2 features, suggesting the embedding of RuO_2 nanodomains within the MnO_2 matrix. Similar to previous observations on Ru-MnO_2, *ex situ* TEM images enable to depict a dynamic picture of the polymer-mediated Ru exsolution and segregation process. After 30 min of oxidation in air, the amorphous PANI coating initially coated on the Ru-MnO_2 surface was significantly reduced (Fig. 3b and 3c). Segregated RuO_2 nanoclusters were clearly seen on the MnO_2 surface, with some detached from the β-MnO_2 surface while still embedded within the amorphous coating (Fig. 3c). As the thermal treatment went on, the polymer coating was mostly pyrolyzed, leaving a relatively condense lattice behind. Meanwhile, the previously extruded nanoclusters were detached from the MnO_2 surface along with the pyrolyzed polymer coating. By the end of the three-hour annealing, a rough surface with a mixed lattice structure was observed on Ru-MnO_2-PT, on which small RuO_2 nanoclusters were distinguishable (Fig. 3d-f). Therefore, through sacrificial pyrolysis the polymer coating helped to anchor the segregated RuO_2 phase to the underlying β-MnO_2 base.

Structural and Electronic Analyses

The electronic structure of pristine β-MnO_2, Ru-MnO_2-T (180 min, omitted hereafter) and Ru-MnO_2-PT (180 min, omitted hereafter) were analyzed using X-ray photoelectron spectroscopy (XPS) and synchrotron-based X-ray absorption spectroscopy (XAS). Prior to that, XRD patterns were acquired (Fig. 4a). Compared to the pristine β-MnO_2, Ru-MnO_2 showed a notable shift of the β-MnO_2(110) plane toward lower 2θ angle (JCPDS 24-0735),[41, 42] corroborating the TEM observation of expanded lattice. After thermal treatment, the MnO_2(110) diffraction peak of Ru-MnO_2-T shifted reversely to higher 2θ angle, which is in line with the contracted lattice seen in TEM images. Additionally, RuO_2 peaks (JCPDS 40-1290) of low intensity can be identified, coinciding with the small RuO_2 crystallites observed by TEM. As for Ru-MnO_2-PT, the 2θ shift of the XRD peaks is negligible when compared to β-MnO_2, suggesting the offset of Ru-induced lattice expansion by polymer-mediated Ru segregation. Meanwhile, peaks of RuO_2 are barely visible due to the inhibited surface oxidation upon Ru segregation, which will be detailed later. No carbon-related diffraction peaks were observed, evidencing the complete pyrolysis of the PANI coating, which was further confirmed by the lack of carbonaceous D and G bands in the Raman spectra (Fig. S14, ESI†).

XPS spectra of Mn 3s splitting (ΔE_{3s}, Fig. 4b), which is caused by electron exchange in the 3s–3d orbitals upon photoelectron ejection and sensitive to the oxidation state of Mn, showed that the Mn valency in Ru-MnO_2-T (~3.9, calculated based on the equation: $AOS_{Mn} = 9.67 - 1.27\Delta E_{3s}$) is close to that of the pristine β-MnO_2 (~4.0).[1, 43, 44] This indicates that the chemical state of Mn in Ru-MnO_2-T, despite of severe surface reconstruction, is mostly saturated. In a stark contrast, the oxidation state of Mn calculated for Ru-MnO_2-PT was only ~ 2.0, suggesting that the pyrolysis of PANI induced a highly reductive Mn state at the surface of the β-MnO_2 nanorods. Correspondingly, XPS O 1s spectra revealed a significantly intensified peak at 531.19 eV for vacancy-related oxygen species (O_v), which indicates an oxygen-deficient lattice structure at the surface of Ru-MnO_2-PT (Fig. 4c). Whereas XPS Ru 3p spectra revealed no signal for the pristine β-MnO_2 as expected, both samples of Ru-MnO_2-T and Ru-MnO_2-PT displayed a strong Ru 3p doublet (Fig. 4d). The binding energies of the Ru peaks for Ru-MnO_2-T are higher than those for Ru-MnO_2-PT by ~0.96 eV, in resonance with the high Mn valency of the former. Therefore, we can conclude that pyrolysis of the PANI coating significantly altered the surface electronic structure of the composite with reduced chemical states of both Ru and Mn.

The above argument was further validated by systematic XAS studies on β-MnO_2, Ru-MnO_2, Ru-MnO_2-T and Ru-MnO_2-PT. X-ray absorption near edge structure (XANES) of Ru K-

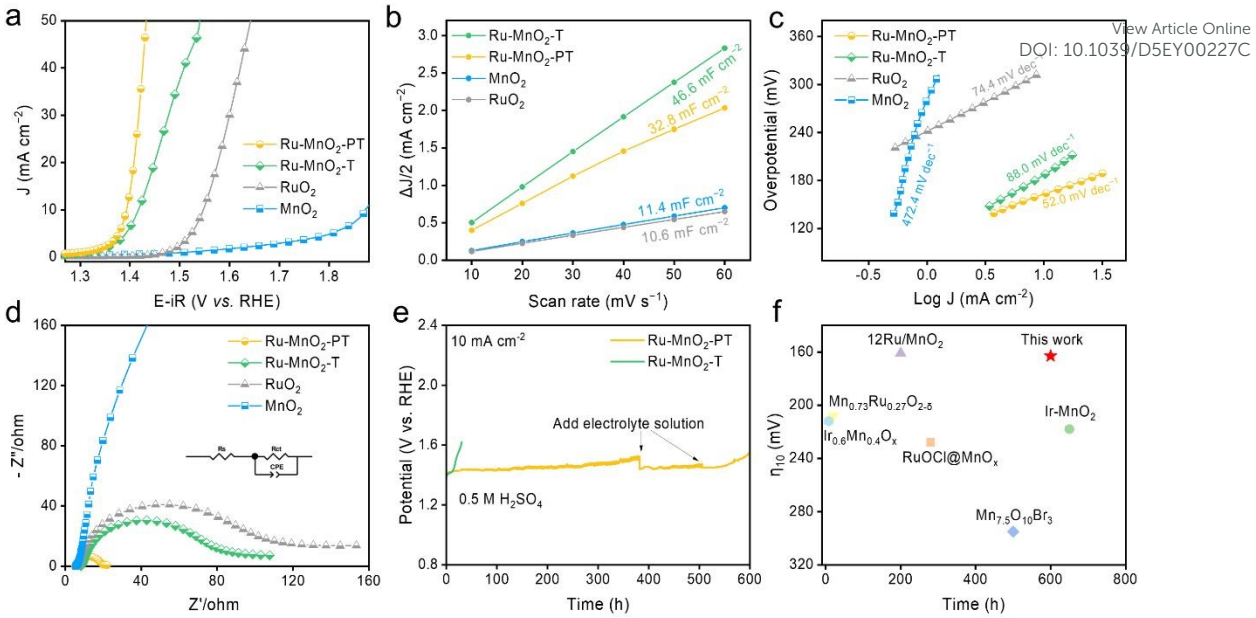

Fig. 5 OER performance metrics of Ru-MnO_2-T and Ru-MnO_2-PT in 0.5 M H_2SO_4 in reference to RuO_2 and β-MnO_2. (a) LSV curves at a scan rate of 10 mV s^{-1}. (b) Measurements of double layer capacitance (C_{dl}) to estimate ECSA. (c) Tafel slopes. (d) EIS spectra taken at 1.45 V. (e) Chronopotentiometric V-t curves at 10 mA cm^{-2}. (f) Comparison of η_{10} and operational stability in the three-electrode cell.

edge showed the photon energy of edge absorption follows the order: Ru-MnO_2-PT < RuO_2 < Ru-MnO_2 < Ru-MnO_2-T (Fig. 4e), echoing the XPS results above. Due to the synthesis involving $KMnO_4$ and the ultrafine RuO_2 crystallites of strong oxophilicity, it was not odd to see both Ru-MnO_2 and Ru-MnO_2-T exhibit even higher formal oxidation numbers than the commercial RuO_2. In the Fourier-transform extended X-ray absorption fine structure in the R space, all samples exhibited a prominent peak at ~1.43 Å (Fig. 4f), which is ascribed to the Ru−O bonding in the first coordination sphere. Consistent with the valency trend, the Ru−O coordination number also follows the order Ru-MnO_2-PT (5.84 ± 0.66) < RuO_2 (6.00 ± 1.43) < Ru-MnO_2 (6.31 ± 0.86) < Ru-MnO_2-T (6.52 ± 0.9) (Fig. S15, Table S2), evidencing that the Ru species in Ru-MnO_2-T are highly oxidized, whereas those in Ru-MnO_2-PT are undercoordinated. Moreover, a small Ru−Ru signal can be discerned at R = 2.28 Å for Ru-MnO_2-PT, suggesting that a small portion of the segregated Ru species might even take the metallic form. This rationalizes the low average valency of Ru in Ru-MnO_2-PT as observed by both XPS and XANES. Based on these spectral findings, we realized that it would be more accurate to refer the segregated Ru phase on the surface of Ru-MnO_2-PT as RuO_x, instead of RuO_2. XANES spectra of Mn K-edge showed the oxidation state of Mn follows the order Ru-MnO_2-PT < Ru-MnO_2-T < MnO_2 (Fig. 4g), coincident with the XPS Mn 3s results. FT-EXAFS spectra in the R space revealed a significantly reduced Mn−O coordination number and suppressed μ-oxo moieties, corroborating the more reductive and chaotic β-MnO_2 lattice induced by PANI pyrolysis.

Taken together from the comprehensive microscopic and spectroscopic characterizations above, we now stand on firm ground to draw an explicit picture on the microstructure and electronic states of Ru-MnO_2-T and Ru-MnO_2-PT: 1) Without PANI coating, segregation of Ru from β-MnO_2 following the Schottky mechanism causes a devastating morphological change while impacting less on the chemical states of Mn and Ru; 2) With PANI coating, Ru segregation concurrent with PANI pyrolysis results in a more coherent surface crystallinity, but at the cost of drastically altered chemical states and electronic structure. Keeping these structural and electronic attributes in mind, we proceed to compare their OER characteristics in acidic medium.

OER characteristics in the three-electrode electrolytic cell

We began by studying the amount of Ru doping on the OER performance of Ru-MnO_2-T. By ramping up the concentration of the $RuCl_3$ precursor in the microwave reaction, we were able to incrementally raise the Ru content in β-MnO_2 from 2.8% to 14.3% (Table S3, ESI†). Adding more $RuCl_3 \cdot 3H_2O$ did not increase the Ru content without altering the morphology and crystallinity of β-MnO_2, as evidenced by the broadened and diminished XRD pattern of $Ru_{14.3\%}$-MnO_2-T (Fig. S16, ESI†). Thus, as aforementioned, we constrained our highest doping quantity not to surpass 15% and abbreviate $Ru_{14.3\%}$-MnO_2-T as Ru-MnO_2-T. Linear sweep voltammetry (LSV) curves taken in 0.5 M H_2SO_4 showed that the OER current density at a given potential increased with the increasing Ru doping as expected (Fig. S17, ESI†), confirming that Ru is indeed responsible for the OER activity.

We then compared the samples of Ru-MnO_2-T and Ru-MnO_2-PT against the commercial RuO_2 benchmark and the β-MnO_2 control. Impressively, Ru-MnO_2-PT exhibited a low overpotential of 163 mV to reach the current density of 10 mA cm^{-2} (η_{10}), which is much superior to that of Ru-MnO_2-T (178 mV), RuO_2 (335 mV) and β-MnO_2 (729 mV) (Fig. 5a). To interrogate the intrinsic activity of the catalysts by excluding the convolution from specific surface area, electrochemical active surface area (ECSA) was estimated by measuring the double layer capacitance (C_{dl}) (Fig. 5b, S18 and Table S4, ESI†). c,

View Article Online
DOI: 10.1039/D5EY00227C

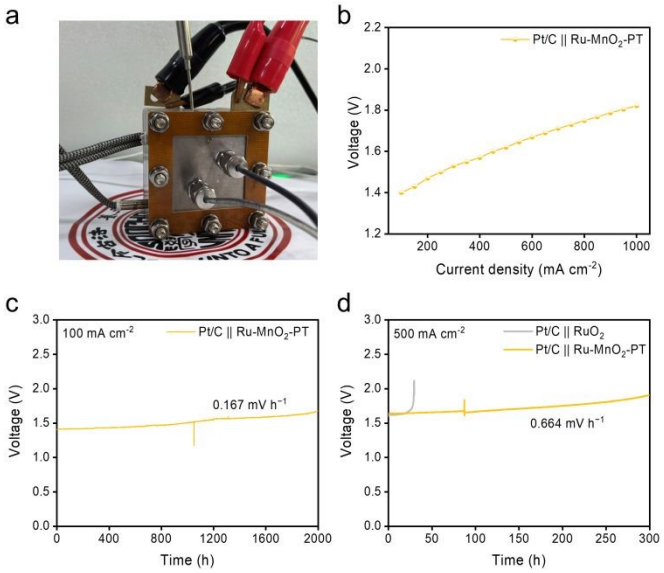

Fig. 6 Performance of Ru-MnO_2-PT in PEMWE. (a) Photograph of the PEMWE device. (b) V-I plot. (c) Chronopotentiometry V-t curve at 100 mA cm^{-2}. (d) Chronopotentiometry V-t curve at 500 mA cm^{-2} acquired on PEMWE utilizing Pt/C and RuO_2 or Ru-MnO_2-PT as the cathode and anode catalysts, respectively.

which is conceivable considering the highly roughened surface Ru-MnO_2-T and Ru-MnO_2-PT due to Ru exsolution and segregation. After normalizing the LSVs to ECSA, both Ru-MnO_2-T and Ru-MnO_2-PT still exhibited a much higher activity than that of RuO_2 (Fig. S19, ESI†), highlighting their superior intrinsic activity and noble metal utilization.

Measurements on the LSV curves near the onset potential revealed a Tafel slope of 52.0 mV dec^{-1} for Ru-MnO_2-PT, followed by RuO_2 (74.4 mV dec^{-1}), Ru-MnO_2-T (88.0 mV dec^{-1}) and β-MnO_2 (472.4 mV dec^{-1}), corroborating the fast electro-kinetics of Ru-MnO_2-PT after minimizing the interference from concentration polarization (Fig. 5c). Electrochemical impedance spectra acquired at 1.45 V under OER conditions revealed a remarkably small charge transfer resistance (R_{ct}) of only 13.2 Ω for Ru-MnO_2-PT, in contrast to those of Ru-MnO_2-T (65 Ω), RuO_2 (144.9 Ω) and β-MnO_2 (1485 Ω) (Fig. 5d). This phenomenon can be partially attributed to the high OV content with improved electric conductivity (Fig. S20, ESI†), and more importantly, the highly active RuOx sites of Ru-MnO2-PT that greatly expedited the electron transport and transfer kinetics. More remarkably, in the three-electrode cell Ru-MnO_2-PT demonstrated a stable operation at 10 mA cm^{-2} for over 600 hours, during which the test was even affected by electrolyte evaporation (Fig. 5e). By contrast, despite the low initial η_{10} (178 mV), Ru-MnO_2-T only lasted for 30 hours before the cathodic potential increased to 1.6 V (Fig. S21, ESI†). We surmise that the loosely stacked RuO_2 nanocrystals segregated from Ru-MnO_2-T might account for its short operational lifetime. Above all, the low η_{10} value of 163 mV, in conjunction with the prolonged operation over 600 hours, ranks Ru-MnO_2-PT one of the most advanced MnO_x-based OER catalysts reported so far (Fig. 5f and Table S5, ESI†).

OER performance in PEMWE

To further validate the practical application of Ru-MnO_2-PT in PEMWE for hydrogen production, both the cathode catalyst (20% Pt/C) and anode catalyst (Ru-MnO_2-PT) were coated onto the Nafion-115 membrane for constructing a membrane electrode assembly operated at 80 ℃ (Fig. 6a, S22 and Table S6, ESI†). In our study, the anode catalyst loading was optimized at 1.5 mg_{Ru} cm^{-2} to assure a stable MEA operation while minimizing the Ru usage. Once the Ru loading reduced from 1.5 to 0.75 mg_{Ru} cm^{-2}, the MEA cell voltage increased from 1.48 to 1.78 V during the 800 h stability test at 100 mA cm^{-2} (Fig. S23).Under the galvanostatic mode, ramping the current density stepwise from 100 to 1000 mA cm^{-2} led to an increase in cell voltage from 1.40 to 1.82 V, attesting to the high activity of the catalysts (Fig. 6b, S24, ESI†). Keeping the operating current density at 100 mA cm^{-2}, the PEMWE was able to operate steadily for over 2000 hours with a voltage degradation rate of only 0.167 mV h^{-1} (Fig. 6c). Further raising the galvanostatic current density to 500 mA cm^{-2}, the cell was still able to sustain a prolonged operation for over 300 hours, exceeding the commercial RuO_2 benchmark and most reported acidic OER catalysts of low noble metal loading (Fig. 6d and Table S5, ESI†). After the prolonged stability test, SEM and TEM images revealed partial dissolution of MnO_2 rods (Fig. S25, ESI†). Post-mortem XPS analysis showed a reduction in the Mn 3s splitting from 6.55 to 6.34 eV, while the Ru 3p peak shifted from 462.3 to 463.0 eV (Fig. S26, ESI†). These changes indicate an increase in the valence states of both Mn and Ru. Consequently, the failure mechanism is attributed to Ru and Mn oxidation to higher valence states, leading to their partial dissolution.[45] Further raising the galvanostatic current density to 1A cm^{-2}, Ru-MnO_2-PT was able to sustain a stable PEMWE operation (4 cm^2 active area) for over 100 h at a low voltage degradation rate of 0.7 mV h^{-1}. Without any iR/HFR correction, the cell voltage increased from 1.80 to 1.87 V at 80 °C under 50 mL min^{-1} water feed, promising for industrial operations (Fig. S27 , ESI†).

Conclusions

In summary, we have successfully developed a high-performance OER catalyst based on MnO_2 with low Ru loading through the thermally driven exsolution and segregation process. Utilizing high-resolution TEM images, we show explicitly the temporal thickening of the segregation layer, comprising a large number of polycrystalline grains formed through the Schottky mechanism. To enhance the cementing of the segregated RuO_x nanocrystals, polyaniline was applied as the sacrificial coating and structural modulator during annealing. The polymer-mediated segregation process resulted in a more condensed surface lattice but significantly altered electronic structure, dramatically reducing the chemical states of Mn and Ru while populating the vacancy-related oxygens. As a result, the best catalyst of Ru-MnO_2-PT achieved a remarkable OER activity in acidic medium, requiring an overpotential of only 163 mV to reach the current density of 10 mA cm^{-2}. Moreover, Ru-MnO_2-PT demonstrated a superb electrocatalytic stability, enabling a prolonged operation of PEMWE for over 2000 hours, exceeding most reported acidic OER catalysts. Through controllably regulating the segregation process of noble metal-doped transition metal oxides, this study offers a novel strategy for the design and fabrication of high-performance OER catalysts with extended durability and alleviated noble metal dependency, paving the way for large-scale deployment of PEMWE systems at reduced cost.

Author contributions

Y. Z., X. Z. and Z. W. contributed equally. Y. Z., Y. P. and Z. D. conceived and designed the studies. Y. Z. and Z. W synthesized the materials, performed their electrochemical properties, analyzed the data and wrote the paper. X. Z. performed the DFT calculations and result analyses. C. W. and X. Z. contributed to the materials synthesis and electrochemical measurements. Y. Z., Z. Z. and M. M. performed the PEM electrolyzer tests, SEM tests, and Raman test. S. M. and D. S. supported the TEM characterization and analysis. X. Y. and T. Z. provided ICP and XRD support. J. Z. supported beamline BL13SSW at Shanghai Synchrotron Radiation Facility for the XAFS. Z. W., Y. P., and Z. D. acquired the financial support for the project. All authors discussed the results and critically reviewed the manuscript.

Conflicts of interest

There are no conflicts to declare.

Data availability

All relevant data are included in the main text and its Supplementary Information.†.

Acknowledgements

This work is supported by Natural Science Foundation of Jiangsu Province (BK20221239, BK20220027), China Postdoctoral Science Foundation (No. 2023M742537), Postdoctoral Fellowship Program of CPSF (No. GZC20231887) and the Priority Academic Program Development (PAPD) of Jiangsu Higher Education Institutions. We also thank for the support from Soochow Municipal laboratory for low carbon technologies and industries. We acknowledge beamline BL13SSW at Shanghai Synchrotron Radiation Facility for the XAFS experiments supports.

Notes and referencess

1 A. Li, S. Kong, K. Adachi, H. Ooka, K. Fushimi, Q. Jiang, H. Ofuchi, S. Hamamoto, M. Oura, K. Higashi, T. Kaneko, T. Uruga, N. Kawamura, D. Hashizume and R. Nakamura, *Science*, 2024, **384**, 666-670.
2 J. Huang, C. N. Borca, T. Huthwelker, N. S. Yüzbasi, D. Baster, M. El Kazzi, C. W. Schneider, T. J. Schmidt and E. Fabbri, *Nat. Commun.*, 2024, **15**, 3067.
3 T. Liu, C. Chen, Z. Pu, Q. Huang, X. Zhang, A. M. Al-Enizi, A. Nafady, S. Huang, D. Chen and S. Mu, *Small*, 2024, **20**, 2405399.
4 J. Cao, D. Zhang, B. Ren, P. Song and W. Xu, *Energy Environ. Sci.*, 2024, **17**, 5911-5921.
5 K. Zhang, X. Liang, L. Wang, K. Sun, Y. Wang, Z. Xie, Q. Wu, X. Bai, M. S. Hamdy, H. Chen and X. Zou, *Nano Res. Energy*, 2022, **1**, 9120032.
6 R. A. Abdelsalam, M. Mohamed, H. E. Z. Farag and E. F. El-Saadany, *Energy Convers. Manage.*, 2024, **319**, 118907.
7 J. Xu, Y. Yang, H. Jin, Y. Zheng and S.-Z. Qiao, *Chem*, 2025, **11**, 102305.
8 R. Qin, G. Chen, X. Feng, J. Weng and Y. Han, *Adv. Sci.*, 2024, **11**, 2309364.
9 X. Wei, S. Sharma, A. Waeber, D. Wen, S. N. Sampathkumar, M. Margni, F. Maréchal and J. Van herle, *Joule*, 2024, **8**, 3347-3372.
10 X. Xiong, J. Tang, Y. Ji, W. Xue, H. Wang, C. Liu, H. Zeng, Y. Dai, H.-J. Peng, T. Zheng, C. Xia, X. Liu and Q. Jiang, *Adv. Energy Mater.*, 2024, **14**, 2304479.
11 S. Ge, R. Xie, B. Huang, Z. Zhang, H. Liu, X. Kang, S. Hu, S. Li, Y. Luo, Q. Yu, J. Wang, G. Chai, L. Guan, H.-M. Cheng and B. Liu, *Energy Environ. Sci.*, 2023, **16**, 3734-3742.
12 C. Lin, J.-L. Li, X. Li, S. Yang, W. Luo, Y. Zhang, S.-H. Kim, D.-H. Kim, S. S. Shinde, Y.-F. Li, Z.-P. Liu, Z. Jiang and J.-H. Lee, *Nat. Catal.*, 2021, **4**, 1012-1023.
13 https://matthey.com/products-and-markets/pgms-and-circularity/pgm-management/).
14 L. Deng, S.-F. Hung, Z.-Y. Lin, Y. Zhang, C. Zhang, Y. Hao, S. Liu, C.-H. Kuo, H.-Y. Chen, J. Peng, J. Wang and S. Peng, *Adv. Mater.*, 2023, **35**, 2305939.
15 X. Ping, Y. Liu, L. Zheng, Y. Song, L. Guo, S. Chen and Z. Wei, *Nat. Commun.*, 2024, **15**, 2501.
16 Q.-Q. Yan, D.-X. Wu, S.-Q. Chu, Z.-Q. Chen, Y. Lin, M.-X. Chen, J. Zhang, X.-J. Wu and H.-W. Liang, *Nat. Commun.*, 2019, **10**, 4977.
17 J. Xu, C.-C. Kao, H. Shen, H. Liu, Y. Zheng and S.-Z. Qiao, *Angew. Chem. Int. Ed.*, 2024, **64**, e202420615.
18 X.-Y. Zhang, H. Yin, C.-C. Dang, H. Nie, Z.-X. Huang, S.-H. Zheng, M. Du, Z.-Y. Gu, J.-M. Cao and X.-L. Wu, *Angew. Chem. Int. Ed.*, 2025, **64**, e202425569.

19 Y. Gao, X. Sun, G. A. M. Mersal, A. Alhadhrami, M. M. Ibrahim, Y. Hou, W. Liu, D. Bildan, H. Algadi and T. X. Liu, *Adv. Compos. Hybrid Mater.*, 2025, **8**, 117.

20 Z. Fan, Z. Luo, X. Huang, B. Li, Y. Chen, J. Wang, Y. Hu and H. Zhang, *J. Am. Chem. Soc.*, 2016, **138**, 1414-1419.

21 Y. Zhang, Z. Li, H. Jang, M. G. Kim, J. Cho, S. Liu, X. Liu and Q. Qin, *Adv. Mater.*, 2025, **37**, 2501586.

22 Z. Yang, Y. Ding, W. Chen, S. Luo, D. Cao, X. Long, L. Xie, X. Zhou, X. Cai, K. Liu, X.-Z. Fu and J.-L. Luo, *Adv. Mater.*, 2025, **37**, 2417777.

23 Y. Cheng, H. Wang, T. Qian and C. Yan, *EnergyChem*, 2022, **4**, 100074.

24 Z. Shi, Y. Wang, J. Li, X. Wang, Y. Wang, Y. Li, W. Xu, Z. Jiang, C. Liu, W. Xing and J. Ge, *Joule*, 2021, **5**, 2164-2176.

25 W. Shi, T. Shen, C. Xing, K. Sun, Q. Yan, W. Niu, X. Yang, J. Li, C. Wei, R. Wang, S. Fu, Y. Yang, L. Xue, J. Chen, S. Cui, X. Hu, K. Xie, X. Xu, S. Duan, Y. Xu and B. Zhang, *Science*, 2025, **387**, 791-796.

26 L. Zhao, Z. Tao, M. You, H. Xiao, S. Wang, W. Ma, Y. Huang, B. He and Q. Chen, *Adv. Sci.*, 2024, **11**, 2309750.

27 J. Oh, S. Joo, C. Lim, H. J. Kim, F. Ciucci, J.-Q. Wang, J. W. Han and G. Kim, *Angew. Chem. Int. Ed.*, 2022, **61**, e202204990.

28 Y. Chen, M. S. Duyar, R. Han, F. He, X. Sun, Y. Chen, W. Liu and J. Liu, *Mater. Today*, 2024, **75**, 259-284.

29 D. Neagu, G. Tsekouras, D. N. Miller, H. Ménard and J. T. S. Irvine, *Nat. Chem.*, 2013, **5**, 916-923.

30 S. Kim, J. Lee, Y. B. Kim, D. Oh, J. K. Kim, B. Koo, H. Kim, G. h. Jung, M. Kim, G. Doo, J. Seo, T. J. Lim, K. Kim, J. W. Han and W. Jung, *ACS Nano*, 2025, **19**, 10026-10037.

31 H. Kim, C. Lim, J. Gu, H. Y. Jeong, J. W. Han, J.-H. Jang and Y. Bu, *Adv. Energy Mater.*, 2024, **14**, 2401307.

32 L. Lv, Z. Yang, K. Chen, C. Wang and Y. Xiong, *Adv. Energy Mater.*, 2019, **9**, 1803358.

33 Z. Li, J. Liu, R. Shi, G. I. N. Waterhouse, X.-D. Wen and T. Zhang, *Adv. Energy Mater.*, 2021, **11**, 2002783.

34 X. Zou, Q. Lu, J. Wu, K. Zhang, M. Tang, B. Wu, S. She, X. Zhang, Z. Shao and L. An, *Adv. Funct. Mater.*, 2024, **34**, 2401134.

35 E. A. Smal, M. N. Simonov, N. V. Mezentseva, T. A. Krieger, T. V. Larina, A. A. Saraev, T. S. Glazneva, A. V. Ishchenko, V. A. Rogov, N. F. Eremeev, E. M. Sadovskaya and V. A. Sadykov, *Appl. Catal. B Environ.*, 2021, **283**, 119656.

36 Y. Luo, D. Zhang, T. Liu, X. Chang, J. Wang, Y. Wang, X.-K. Gu and M. Ding, *Adv. Funct. Mater.*, 2024, **34**, 2403922.

37 S. Moxon, J. Skelton, J. S. Tse, J. Flitcroft, A. Togo, D. J. Cooke, E. Lora da Silva, R. M. Harker, M. T. Storr, S. C. Parker and M. Molinari, *J. Mater. Chem. A*, 2022, **10**, 1861-1875.

38 L.-Y. Meng, B. Wang, M.-G. Ma and K.-L. Lin, *Materials Today Chemistry*, 2016, **1**, 63-83.

39 R. Nagahata and K. Takeuchi, *The Chemical Record*, 2019, **19**, 51-64.

40 W. Schottky, *Z. Phys. Chem. B*, 1935, **29**, 335.

41 Y. Qin, Y. Liu, Y. Zhang, Y. Gu, Y. Lian, Y. Su, J. Hu, X. Zhao, Y. Peng, K. Feng, J. Zhong, M. H. Rummeli and Z. Deng, *ACS Catal.*, 2023, **13**, 256-266.

42 H. Li, H. Yao, X. Sun, C. Sheng, W. Zhao, J. Wu, S. Chu, Z. Liu, S. Guo and H. Zhou, *Chem. Eng. J.*, 2022, **446**, 137205.

43 E. S. Ilton, J. E. Post, P. J. Heaney, F. T. Ling and S. N. Kerisit, *Appl. Surf. Sci.*, 2016, **366**, 475-485.

44 M. C. Biesinger, B. P. Payne, A. P. Grosvenor, L. W. M. Lau, A. R. Gerson and R. S. C. Smart, *Appl. Surf. Sci.*, 2011, **257**, 2717-2730.

45 L. Wang, Q. Pan, X. Liang and X. Zou, *ChemSusChem*, 2025, **18**, e202401220.

View Article Online
DOI: 10.1039/D5EY00227C

Data availability

All relevant data are included in the main text and its Supplementary Information.†.